This is the peer-reviewed, final accepted version for American Mineralogist, published by the Mineralogical Society of America.
The published version is subject to change. Cite as Authors (Year) Title. American Mineralogist, in press.
DOI: https://doi.org/10.2138/am-2022-8471. http://www.minsocam.org/

Revision 2:
Correlations between cathodoluminescence intensity and aluminum concentration in low-temperature hydrothermal quartz

Mao-Wen Yuan[a,b], Lin Li[a,c,*], Masroor Alam[d], M. Santosh[b,e], Sheng-Rong Li[a,b], Zeng-Qian Hou[f]

[a]*State Key Laboratory of Geological Processes and Mineral Resources, China University of Geosciences, Beijing 100083, China*

[b]*School of Earth Science and Resources, China University of Geosciences, Beijing 100083, China*

[c]*Institute of Earth Sciences, China University of Geosciences, Beijing 100083, China*

[d]*Department of Earth Sciences, Karakoram International University Gilgit 15100 Pakistan*

[e]*Department of Earth Sciences, University of Adelaide, SA 5005, Australia*

[f]*Institute of Geology, Chinese Academy of Geological Sciences, Beijing 100037, China*

ABSTRACT:

Quartz cathodoluminescence (CL) images are commonly combined with trace element concentrations to decipher complex histories of hydrothermal systems. However, the correlations between aluminum content and CL zoning of low-temperature hydrothermal quartz and their genesis remain controversial. In this contribution, a multiparametric study was carried out on CL-aluminum zoning of low-temperature hydrothermal quartz (<350°C) from the Shihu and Rushan quartz-vein type Au deposits in the North China Craton. The results show that aluminum concentration correlates negatively with CL intensity in quartz from the Shihu Au deposit. CL-dark quartz zoning has significant Al concentrations as well as detectable Al-H bonds. However, in the Rushan Au deposit, the correlation is positive, and aluminum is enriched in the CL-bright quartz zoning. The Al content is positively correlated with K content with r^2=0.769. Combined with the electron backscatter diffraction (EBSD), X-ray single crystal diffraction (XRD) and transmission electron microscope (TEM) data, we infer that the genesis of CL zoning in the low-temperature hydrothermal quartz is closely related to Al^{3+}-H^+ and Al^{3+}-K^+ concentrations. The Al^{3+}-K^+ may act as the CL-activator, while the Al^{3+}-H^+ may act as the CL-dampener. Where Al^{3+}-Si^{4+} substitution is charge balanced by hydrogen, the intensity of CL response decreases; where Al^{3+}-Si^{4+} substitution is charge balanced by potassium, the intensity of CL response increases. The correlations between CL intensity and aluminum concentration in the low-temperature hydrothermal quartz reflect pH fluctuations of hydrothermal system.

KEY WORDS: Shihu and Rushan Au deposits; Low-temperature hydrothermal quartz; Cathodoluminescence; Al^{3+}-H^+ and Al^{3+}-K^+ concentrations; pH

1. Introduction

Cathodoluminescence (CL) images can effectively visualize the micro-textures that record complex history of quartz precipitation and dissolution (Rusk and Reed 2002; Götze et al. 2001, 2005; Olivia et al. 2020). Concentrations of trace elements reflect the growth process and physio-chemical conditions during quartz growth such as pressure, temperature and pH (Wark and Watson 2006; Thomas et al. 2010; Acosta et al. 2020). Therefore, CL images combined with trace element concentrations in quartz are extensively used to obtain insight into quartz vein formation processes, especially in magmatic systems (Watt et al. 1997; Penniston-Dorland 2001; Monecke et al. 2002; Redmond et al. 2004). Müller et al. (2005) used CL zones of quartz to reveal multiple magma mixing process in the eastern Erzgebirge volcano-plutonic complex (Germany, Czech Republic). Allan and Yardley (2007) used scanned CL and trace elements of quartz to track the meteoric infiltration into a magmatic-hydrothermal system in the Mt. Leyshon, porphyry deposit, Australia. Takashi et al. (2020) evaluated the cooling processes of the Toki granitic pluton by using (CL) oscillatory-zoned quartz. Such studies have helped to better understand the magmatic processes, origin of granites and genesis of porphyry deposit (Watt et al. 1997; Müller et al. 2005; Takashi et al. 2020). However, there is lack of the application on the low-temperature hydrothermal deposits due to the controversy on the genesis of CL zoning.

Several studies have explored the coupling relationships between CL intensity and trace element concentrations in quartz crystals (Müller et al. 2000, 2002; Penniston-Dorland 2001; Rusk et al., 2011). The formation process of CL-trace element zoning in high-temperature quartz (>350°C; Rusk et al. 2008) shows that CL intensity variations in the high-temperature quartz are positively correlated with the trace element concentrations, such as Ti, Al, K, Na, H, Li and P (Götze et al. 2004; Landtwing and Pettke 2005; Wang et al. 2022). The genesis of CL zoning of the low-temperature hydrothermal quartz (<350°C; Rusk et al. 2008; Qiu et al. 2021) is different from that of the high-temperature quartz and demonstrably more complex. Correlations between CL intensity and trace elements in the low-temperature hydrothermal quartz are varied. For example, in most of low-temperature hydrothermal quartz (such as quartz in the Magmont, Comstock Lode and Butte Main Stage deposits; Rusk et al. 2008), aluminum concentration correlates positively with CL intensity, but in some low-temperature hydrothermal quartz (such as quartz in the Red Dog and Jerritt Canyon deposits; Rusk et al. 2008), aluminum concentrations and CL intensities are inversely correlated. These variations in correlation greatly affects our understanding of the genesis and implications of low-temperature hydrothermal quartz and raises several questions such as which factors control the correlations between CL intensity and aluminum concentration in the low-temperature hydrothermal quartz, and what are the geological processes. In this contribution, it is necessary to carry out a detailed mineralogical study on the genesis of low-temperature hydrothermal quartz cathodeluminescence zoning to reveal the correlation between CL intensity and trace element concentration in the low-temperature hydrothermal quartz and its geological implications.

In the present study, we have integrated scanning electron microscope cathodoluminescence (SEM-CL), electron microprobe (EMP), electron backscatter diffraction (EBSD), X-ray single crystal diffraction (XRD), Fourier transform infrared spectroscopy (FTIR) and transmission electron microscope (TEM) data of quartz from the Shihu and Rushan Au deposits in the North China Craton (NCC) to evaluate the genesis of CL-aluminum zoning in low-temperature hydrothermal quartz and the implications for the evolution of hydrothermal system. Our results provide a new understanding of the genetic relation between the CL-aluminum zoning of low-temperature hydrothermal quartz and hydrothermal pH.

2. Sampling and analytical methodology

The Rushan Au deposit, hosted by the Mesozoic granitoids in the middle part of the Muping-Rushan gold belt in the Jiaodong Peninsula of eastern North China Craton (NCC), is currently the largest lode gold deposit in terms of a single vein Au resource (>30t) in China (Fig. 1a, b; Goldfarb and Santosh 2014; Li and Santosh 2017; Deng et al. 2017, 2020a, 2020b; Qiu et al. 2020a, 2020b; Li et al. 2022). The Shihu Au deposit, located in the Fuping district of the northern Taihang Mountain, is the largest gold deposit (>40t) in the central North China Craton (Fig. 1a, d; Li et al. 2013; Zeng et al. 2019). Both deposits show similar mechanisms of ore genesis (Hou et al. 2017; Deng et al. 2020c; Li et al. 2020; Yu et al. 2022). The auriferous quartz-sulfide veins from both deposits contain numerous coarse-grained quartz crystals with regular zoning structure (Li et al. 1994; Zeng 2019; Feng et al. 2022). The zoned quartz is thought to have formed in the early ore-forming stage of mineralization with homogenous temperatures of 260-310℃ (Rushan; pyrite-quartz stage; Cao 2013; Sai et al. 2020) and 268-331℃ (Shihu; pyrite-quartz stage; Zeng 2019) based on fluid inclusion data, which are consistent with the low-temperature quartz defined by Rusk et al. (2008, 2011) (<350℃).

Fifteen ore samples containing zoned quartz from the elevation 635 m of No. II orebody in the Rushan Au deposit (Fig. 1c) and thirteen ore samples from the elevation 300 m of No. 101 orebody in the Shihu Au deposit (Fig. 1e) were collected for this study. All the zoned quartz samples were polished to make thin sections and prepared for SEM-CL, EMP and EBSD analysis. Hundreds of SEM-CL images were taken and merged into a complete picture to reveal quartz CL zoning and to carry out EMP and EBSD mapping (Fig. 3, 4; Supplementary material). Small quartz grains (diameter ~40μm) of different CL zoning were picked out from the thin sections for XRD and FTIR analyses (analyzed locations are shown in Fig. 4). Two quartz ultra-thin sections from the aluminum-rich bands were prepared for TEM analysis (analyzed locations are shown in Fig. 5).

The scanning electron microscope cathodoluminescence (SEM-CL) images were acquired at the State Key Laboratory of Biogeology and Environmental Geology, China University of Geosciences (Beijing) using a Zeiss Supra 55 field emission scanning electron microscope (FESEM) equipped with a Gatan ChromaCL2 cathodoluminescence (CL) detector. Platinum-coated, polished sections were analyzed at 10 kV with beam current from 1 to 40 nA. The SEM-EBSD analysis was carried out by a Zeiss Signma scanning electron microscope (SEM) coupled with a HKL Nordlys Nano electron backscattered diffraction (EBSD) detector at the Institute of Geology, China Earthquake Administration, China (Yang et al. 2019). Crystal orientation images covering the quartz grains were obtained with a step size of 1 μm (Shihu) and 5 μm (Rushan) using the Oxford Instruments HKL AZtec software. A working distance of 18.4 mm was used for pattern acquisition and automatic indexing was performed using the AZtec software. The CHANNEL 5 software was used for noise reduction and for filling the missing data with at least 8 identical neighbors with

DOI: https://doi.org/10.2138/am-2022-8471. http://www.minsocam.org/

similar orientation. The resulting EBSD data was optimized using MTex to remove points with large angular deviation and to smooth intra-crystalline date (Bachmann et al. 2010; Henry et al. 2017).

The major and trace element compositions of the hydrothermal quartz were analyzed by a JXA-8230 electron microprobe (EMP) (Beijing GeoAnalysis Co., Ltd.,). Operating conditions included 20kV accelerating voltage, the beam diameter of 5μm and a beam current of 20nA. Standard substances for analysis refer to GB/T 15,074-2008 general rules. The EPMA X-ray elemental maps were determined at the Beijing GeoAnalysis Co., Ltd., using a 4 WDS detector-equipped Camaca SX100 electron microprobe. Operating conditions were 250-300ms dwell time per spot, 80nA beam current and 20kV acceleration. Aluminum, Ti, Si, K, Na, Ga and Ge were analyzed by wavelength dispersive spectroscopy (WDS). Elemental maps are up to 256×256 pixels in size, with 1-2μm steps (distance between analysis spots, or spatial definition). All EMP spot analyzed results and analyzed locations are listed in the Supplementary material Table. S1 and attached figures.

X-ray single crystal diffraction (XRD) analyses were carried out at the State Key Laboratory of Geological Processes and Mineral Resources, China University of Geosciences (Beijing), China using a Rigaku Oxford XtaLAB PRO-007HF microfocus rotating anode X-ray source (1.2kW, MoKα, λ=0.71073Å) and a hybrid pixel array detector single-crystal diffractometer. The X-ray powder diffraction data were recorded with a diffractometer using MoKα radiation. The scanning speed and range of each sample are listed in the Supplementary material Table. S2. The cell volume and a_0 values of quartz are obtained from the CIF documents using Mercury software, which are listed in the Supplementary material Table. S3.

Fourier transform infrared spectroscopy (FTIR) analyses were carried out at the State Key Laboratory of Geological Processes and Mineral Resources, China University of Geosciences (Beijing), China, using a TENSOR 37 FTIR equipped with a Rocksol1D^{TM} interferometer and Digi tect^{TM} detector, with working voltage of 12 kV, a current of 10 A. The detected spectral range is from 7800cm^{-1} to 370cm^{-1}. The

DOI: https://doi.org/10.2138/am-2022-8471. http://www.minsocam.org/

wavenumber accuracy is better than 0.01 cm^{-1}. Standard resolution is 0.6cm^{-1} with an option for 0.3cm^{-1}. Small quartz grains (diameter ~50μm) picked out from aluminum-rich bands in the thin sections (as shown in Fig. 4) were prepared for FTIR analyses. These grains were ground to a 200-mesh powder in an agate mortar, and then dried to eliminate the influence of inclusions in quartz on the test results. One mg quartz sample was thoroughly mixed with 200 mg KBr (200 mesh, prebaked in an infrared oven for 24 hours) and a hydraulic press was used to make 0.03mm thin section for FTIR analysis. The FTIR data were processed by Origin 2017 software.

The transmission electron microscope (TEM) and high-resolution transmission electron microscopy (HRTEM) analyses were carried out by a FEI Tecnai F20 transmission electron microscope (TEM) in the Shiyanjia Lab (www.shiyanjia.com). A ZEISS Crossbeam 540 (Focused Ion beam-SEM) was used to pick out ultra-thin sections from the aluminum-rich bands of quartz from the Rushan and Shihu Au deposits for TEM and HRTEM analyses.

3. Results and Discussion

3.1 Correlations between aluminum and CL intensity

Correlations between CL intensity and aluminum concentration of quartz from the Shihu and Rushan Au deposits are distinctly different. In the Shihu Au deposit, aluminum concentration and CL intensities of quartz are negatively correlated, whereas in the Rushan Au deposit, aluminum concentration correlates positively with the CL intensity. The EMP spot analyses show that in the zoned quartz from Shihu Au deposit, aluminum concentrations in the CL-bright zone are mostly lower than that of the CL-dark zone (>0.4 wt%) (Fig. 3b), and the aluminum concentration shows lack of any correlation with potassium content with r^2=0.014 (Fig. 2a). However, in the zoned quartz from Rushan Au deposit, the CL-bright zone mainly shows higher aluminum concentration (>0.2 wt%) than that of the CL-dark zone (<0.1 wt%), and the aluminum concentration positively correlates with the potassium concentration with r^2=0.769 (Fig. 2b, 3b).

The correlations between aluminum concentration and CL intensity of quartz from the Shihu and Rushan Au deposits are well demonstrated in the EMP element maps. A good correspondence between CL-dark band and aluminum-rich band in the quartz from the Shihu Au deposit is presented (Fig. 3b, 4). Conversely, in the quartz from the Rushan Au deposit, the aluminum-rich band well corresponds to the CL-bright band (Fig. 3b, 4). It can be seen that the intensity of CL decreases with increasing aluminum content in the quartz of the Shihu Au deposit, while that of the Rushan Au deposit is on the contrary. The distribution of potassium in quartz from the Rushan Au deposit shows obvious zonal structure, which has good correspondence with the CL zoning and aluminum zoning (Fig. 4). However, in the Shihu Au deposit, no potassium zoning was detected in quartz. Instead, considerable Al-H bonds are detected in the aluminum-rich quartz zoning (CL-dark quartz zoning), which is obviously more enriched than that of quartz in the Rushan Au deposit (Fig. 4).

3.2 Crystallographic properties of different quartz CL zoning

Previous studies have demonstrated that Al^{3+} substitutes Si^{4+} in the quartz structure with charge compensation by additional ions (such as H^+, Li^+, Na^+ and K^+) in interstitial sites related to structural channels (Götze et al. 2001; Larsen et al. 2004; Landtwing and Pettke 2005). The correlations between CL intensity vs. Al concentration and Al vs. K, as well as FTIR characteristics of quartz suggest the substitution of Al^{3+}, K^+ and $H^+$for Si^{4+} in the quartz structure of the Shihu and Rushan Au deposits (Fig. 2, 3b, 4; Landtwing and Pettke 2005; Naoya et al. 2005; Rusk et al. 2008). Due to the larger ionic radius of K^+ than that of H^+ and Li^+, the effect of K^+ incorporation on lattice structure (cell volume and a_0) of quartz should be much greater than that of H^+ and Li^+ incorporation (Allan and Yardley 2007). The X-ray single crystal diffraction analyses shows the variations of crystal cell parameters between CL-dark zone and CL-bright zone in the Shihu and Rushan Au deposits (Fig. 4). In the Shihu Au deposit, the cell volume and a_0 values of the CL-bright zone and

DOI: https://doi.org/10.2138/am-2022-8471. http://www.minsocam.org/

CL-dark zone (Al and H rich band) are almost same, which are within 112 Å^3 to 112.5 Å^3 and 4.9 Å to 4.91 Å (Fig. 4). However, in the quartz from the Rushan Au deposit, the cell volume and a_0 values of the CL-bright zone are obviously lager than those of the CL-dark zone (Fig. 4). The a_0 value increases from 4.89 Å in the CL-dark zone to 4.95 Å in the CL-bright zone (Al- and K-rich quartz zone). Meanwhile, the cell volume increases from 112.1 Å^3 in the CL-dark zoning to 115.4 Å^3 in the CL-bright zoning (Fig. 4). Comparing the samples from two deposits, the cell volume and a_0 values of the Al-rich quartz zone from Rushan Au deposit are obviously lager than those of Shihu Au deposit. These results confirm that (Al^{3+}-K^+)-Si^{4+} substitution in the quartz from Rushan Au deposit shows more obvious lattice distortion than that of (Al^{3+}-H^+)-Si^{4+}substitution in quartz from the Shihu Au deposit. Systematically, these distortions of lattice structure may cause significant crystal deformation in quartz from the Rushan Au deposit (Passchier and Trouw 2005). In this contribution, two quartz grains containing both CL-dark and CL-bright zones from the Shihu and Rushan Au deposits were selected to carry out EBSD analysis to visualize the deformation distribution (Fig. 3a, b). The band contrast (BC) images show that all captured pattern images of quartz have high image quality (Fig. 3c). Thus, the results of deformation distribution of analyzed quartz are reliable. The inverse pole figure (IPF) colouring images show that the quartz from the Shihu Au preferred crystal orientation of "a" faceprojected along the Y direction, while the quartz from the Rushan Au deposit has two crystal orientations, termed as "r" and "m" faces (Fig. 3d), indicating different degrees of deformation of the quartz crystals from two deposits (Ghosh et al. 2017). The uniform distribution of kernel average misorientation (KAM) and grain reference orientation deviation (GROD) angle in the quartz from the Shihu Au deposit indicate that the crystal is almost undeformed and its crystal structure may not have changed (Fig. 3e, f; Ghosh et al. 2017; Kleber et al. 2021). However, in the Rushan Au deposit, the CL-bright band of quartz obviously presents deformation characteristics, seen in different colors in the KAM and GROD angle maps (Fig. 3e, f), and suggesting that CL-bright quartz from the Rushan Au deposit may have deformed (Ghosh et al. 2017; Sai et al. 2020; Kleber et al. 2021). The transmission electron

DOI: https://doi.org/10.2138/am-2022-8471. http://www.minsocam.org/

microscopy (TEM) results confirm that both bright and dark zones in quartz from the Shihu Au deposit display regular lattice stripes and no obvious lattice defects are found (Fig. 5a, b). However, in the Rushan Au deposit, the aluminum-rich CL-bright quartz zoning obviously shows considerable lattice defects (Fig. 5c, d), which might be related to the Al^{3+}-K^{+} substitution for Si^{4+} (Fig. 2b, 5e, f) (Hochella et al. 2008; Yu et al. 2021). Combing the correlations between Al concentration vs. CL intensity and Al vs. K, as well as FTIR, XRD, EBSD, TEM analysis results, we consider that the genesis of CL zoning in the low-temperature hydrothermal quartz is closely related to (Al^{3+}-K^{+})-Si^{4+} and (Al^{3+}-H^{+})-Si^{4+} substitutions in quartz lattice. The negative correlation between CL intensity and aluminum concentration in quartz of the Shihu Au deposit are closely related to the Al^{3+}-H^{+} substitution for Si^{4+}(Fig. 5g), while the positive correlation in quartz of the Rushan Au deposit is more likely to depend on the Al^{3+}-K^{+} substitution for Si^{4+}(Fig. 5h). The Al^{3+}-K^{+} may act as the CL-activator, while the Al^{3+}-H^{+} may act as the CL-dampener. Where aluminum substitution is charge balanced by hydrogen, the intensity of CL response decreases; where aluminum substitution is charge balanced by potassium, the intensity of CL response increases.

4. Forming conditions of CL-aluminum zoning

Variability in quartz CL intensity as observed relates to trace-element concentrations that could result from changes in fluid chemistry, pressure and temperature during quartz crystallization (Landtwing and Pettke 2005; Naoya et al. 2005; Wang et al. 2021). The quartz CL zoning reported in this study is thought to have formed in a narrow range of formation temperature with homogenous temperatures of 260-310℃ (Rushan; Li et al. 1992; Li et al. 1994; Cao 2013; Sai and Qiu 2020) and 268-331℃ (Shihu; Ao 2009; Zeng 2019). Different quartz CL zoning forms within similar temperature ranges (Cao 2013; Zeng 2019). Sharp contrasts in aluminum concentration from zone to zone in single quartz grain, where no evidence of temperature change exists, suggest that CL-aluminum zoning in quartz does not develop due to temperature fluctuations (Rusk et al. 2008). Pressure fluctuation has a strong influence on quartz solubility and thus the reaction affinity of quartz precipitation. Hu et al. (2005) pointed out that the mineralization pressure of Rushan Au deposit fluctuated from 92 MPa to 269 MPa (Hu et al., 2005). Cao (2013) indicated that the mineralization pressure of Shihu Au deposit ranges from 55MPa to 95MPa (Cao, 2013). The wide ranges of mineralization pressure in the two deposits reflect the process of fluid pulsation during the formation of quartz veins, which might result in the formation of quartz zones related to the frequency of fluid pulsation (Li et al., 1994; Cao, 2013). On these basics, the fluctuation of mineralization pressure seems to have a certain contribution to the formation of quartz CL zoning. However, this conclusion cannot be drawn from the experimental data presented in this paper unless detailed fluid inclusion studies are performed on different quartz CL zoning.

Previous studies noted that although aluminum concentration in hydrothermal quartz is incapable of reflecting the temperature of quartz precipitation, it is a good indicator of aluminum solubility, which is strongly dependent on pH (Rusk et al. 2008). Generally, with decreasing pH, aluminum solubility increases (Luo et al. 2001). Thus, both the CL-dark (Al-rich) quartz in the Shihu Au deposit and CL-bright (Al-rich) quartz in the Rushan Au deposit are considered to have formed under an acidic environment. The higher aluminum concentration in CL-bright quartz in the Shihu Au deposit (Fig. 2 and Fig. 4e, f) suggests that the crystallization conditions for CL-dark quartz from the Shihu deposit were more acidic then those of CL-bright quartz from the Rushan Au deposit (Luo et al. 2001; Rusk et al. 2008), which is also confirmed by considerable Al-H bonds detected in the quartz zoning. The widespread distribution of K-feldspar alteration zones in the Rushan Au deposit (Li et al. 2013, 2015; Deng et al. 2020c) indicates that potassium in the ore-forming hydrothermal fluids was consumed in large quantities. Potassium concentration in the solution might be mostly affected by the solubility of potassium feldspar, which is strongly dependent on pH (Luo et al. 2001). Generally, with the decrease of pH value, potassium feldspar solubility increases significantly (Luo et al. 2001). However, in strong acidic environment, H^+ may replace K^+ to compensate the charge of Al^{3+}-Si^{4+} substitution (Landtwing and

DOI: https://doi.org/10.2138/am-2022-8471. http://www.minsocam.org/

Pettke 2005; Naoya et al. 2005). Zhu (1991) obtained the fluid pH values of different mineralization stages in the Rushan Au deposit (4.50 ~ 5.76). Shen et al. (2000) indicated that pH of ore-forming fluid of the Rushan Au deposit ranged from 5 to 6. Combing with our study, we consider that the formation of CL-bright quartz from the Rushan Au deposit is more likely related to an intermediate-acidic environment. Therefore, aluminum-rich quartz zoning in the Shihu and Rushan Au deposits were formed in acidic and intermediate-acidic environments, respectively, which are obviously different from the neutral environment of aluminum deficient quartz zoning. The formation of CL-aluminum zoning in quartz from the Shihu and Rushan Au deposits might have been caused by pH fluctuation of the hydrothermal fluid.

ACKNOWLEDGMENTS

We greatly appreciate associate editor Prof. Jianwei Wang, Tech Team of American Mineralogist, two reviewers (Prof. Marisa Acosta and one anonymous reviewer) and Prof. Jun Deng for their insightful and constructive comments and suggestions which greatly helped improving this paper. This research was financially supported by the National Natural Science Foundation of China (grant no. 91962101, 41872038, 42130801), Ministry of Science and Technology of China (grant no. 2016YFC0600106).

References

Acosta, M.D., Watkins, J.M., Reed, M.H., Donovan, J.J., and DePaolo, D.J. (2020) Ti-in-quartz: Evaluating the role of kinetics in high temperature crystal growth experiments. Geochimica et Cosmochimica Acta, 281, 149–167.

Allan, M.M. and Yardley, B.W.D. (2007) Tracking meteoric water infi ltration into a magmatic hydrothermal system: A cathodoluminescence, oxygen isotope, and trace element study of quartz from Mt. Leyshon, Australia. Chemical Geology, 240, 343–360.

Ao, Z. (2009) The genetic mineralogy and deep forecast of the Lingshou Shihu gold mine in

Hebei. Ph.D. thesis. China University of Geosciences, Beijing (in Chinese with English abstract).

Bachmann, F., Hielscher, R., and Schaeben, H. (2010) Texture analysis with MTEX–free and open source software toolbox. Solid State Phenom, 160, 63–68.

Cao, H. (2013) Characteristics of mineralization mineralogy in the Great depth of Jinqingding gold deposit, Jiao Dong Region. Ph.D. thesis. China University of Geosciences, Beijing (in Chinese with English abstract).

Deng, J., Wang, Q., and Li, G.J. (2017) Tectonic evolution, superimposed orogeny, and composite metallogenic system in China. Gondwana Research, 50, 216–266.

Deng, J., Yang, L.Q., Groves, D.I., Zhang, L., Qiu, K.F., and Wang, Q.F. (2020a) An integrated mineral system model for the gold deposits of the giant Jiaodong province, eastern China. Earth-Science Reviews, 208, 103274.

Deng, J., Wang, Q., Santosh, M., Liu, X.F., Liang, Y.Y., Yang, L.Q., Zhao, R., and Yang, L. (2020b) Remobilization of metasomatized mantle lithosphere: a new model for the Jiaodong gold province, eastern China. Mineralium Deposita, 55, 257–274.

Deng, J., Qiu, K.F., Wang, Q.F., Goldfarb, R.J., Yang, L.Q., Zi, J.W., Geng, J,Z., and Ma, Y. (2020c) In situ dating of hydrothermal monazite and implications for the geodynamic controls on ore formation in the Jiaodong gold Province, eastern China. Economic Geology, 115(3), 671–685.

Feng, Y.C., Qiu, K.F., Wang, D.Z., Sha, W.J., and Li, S., 2022. Forming conditions of tellurides and their constraints on gold enrichment in Linglong gold district, Jiaodong gold province. Acta Petrologica Sinica, 38(1): 63-77 (in Chinese with English abstract).

Ghosh, B., Misra, S., and Morishita, T. (2017) Plastic deformation and post-deformation annealing in chromite: Mechanisms and implications. American Mineralogist, 102(1), 216-226.

Goldfarb, R.J. and Santosh, M. (2014) The dilemma of the Jiaodong gold deposits: are they unique? Geoscience Frontiers, 5, 139–153.

Götze, J., Plotze, M., and Habermann, D. (2001) Origin, spectral characteristics and practical applications of the cathodolumimescence (CL) of quartz-a review. Mineralogy and Petrology, 71, 225–250.

Götze, J., Plötze, M., and Trautmann, T. (2005) Structure and luminescence characteristics of quartz from pegmatites. American Mineralogist, 90, 13–21.

Götze, J., Plötze, M., Graupner, T., Hallbauer, D.K., and Bray, C.J. (2004) Trace element incorporation into quartz: A combined study by ICP-MS, electron spin resonance, cathodoluminescence, capillary ion analysis, and gas chromatography. Geochimica et Cosmochimica Acta, 68, 3741–3759.

Henry, H., Tilhac, R., Griffin, W.L., O'Reilly, S.Y., Satsukawa, T., Kaczmarek, M.-A., Grégoire, M., and Ceuleneer, G. (2017) Deformation of mantle pyroxenites provides clues to geodynamic processes in subduction zones: case study of the Cabo Ortegal Complex, Spain. Earth and Planetary Science Letters, 472, 174–185.

Hochella, J.M.F., Lower, S.K., Maurice, P.A., Penn, R.L., Sahai, N., Donald L.S., and Benjamin, S.T. (2008) Nanominerals, Mineral Nanoparticles, and Earth Systems. Science, 319(5870), 1631-1635.

Hou, Z.Q., Zhou, Y., Wang, R., Zheng, Y.C., He, W.Y., Zhao, M., Evans, N.J., and Weinberg, R.F. (2017) Recycling of metal-fertilized lower continental crust: Origin of non-arc Au-rich porphyry deposits at cratonic edges. Geology, 45(6), 563–566.

Hu, F.F., Fan, H.R., Shen, K., Zhai, M.G., Jin, C. W., and Chen, X.S. (2005) Nature and evolution of ore-forming fluids in the Rushan lode gold deposit, Jiaodong Peninsula of eastern China. Acta Petrologica Sinica, 21(5), 1329-1338. (In Chinese with English abstract)

Kleber, F.P., Leonardo, E.L., Jeferson, L.B., Dayanede, C.M., Mariana, D.G.P.B., Bruna, G.D., Nicole, P.H., and Selmo, C.K. (2021) Alkali-silica reaction (ASR)-Investigation of crystallographic parameters of natural sands by backscattered electron diffraction. IBRACON Structures and Materials Journal, 14(3), e14308.

Landtwing, M. and Pettke, T. (2005) Relationships between SEM-cathodolumines- cence response and trace element composition of hydrothermal vein quartz. American Mineralogist, 90, 122-131.

Larsen, R.B., Henderson, I., Ihlen, P.M., Francois, J. (2004) Distribution and petrogenetic behaviour of trace elements in granitic pegmatite quartz from South Norway. Contributions to Mineralogy and Petrology, 147(5), 615-628.

Li, S.R. and Santosh. M. (2017) Geodynamics of heterogeneous gold mineralization in the North China Craton and its relationship to lithospheric destruction. Gondwana Research, 50, 267-292.

Li, L., Santosh, M., and Li, S. R. (2015). The 'Jiaodong type' gold deposits: Characteristics, origin and prospecting. Ore Geology Reviews, 65, 589–611.

Li, L., Li, C., Li, Q., Yuan, M.W., Zhang, J.Q., Li, S.R., M. Santosh., Shen, J.F., and Zhang, H.F. (2022) Indicators of decratonic gold mineralization in the North China Craton. Earth-Science Reviews, https://doi.org/10.1016/j.earscirev.2022.103995.

Li, S.R., Santosh, M., Zhang, H.F., Shen, J.F., Dong, G.C., Wang, J., and Zhang, J.Q. (2013) Inhomogeneous lithospheric thinning in the central North China Craton: Zircon U–Pb and S–He–Ar isotopic record from magmatism and metallogeny in the Taihang Mountains. Gondwana Research, 23, 141–160.

Li, S.R, Chen, G.Y., Shao, W., and Sun, D.S. (1994) A study on the application of zoning structure of quartz in mineralogical mapping. Acta Mineralogical Sinica, 14(4), 378-382.(In Chinese with English abstract)

Li, S.R, Santosh, M., and Yang, C.X. (2020) Heterogeneous gold metallogeny in the North China Craton. Geological Journal, 55, 5641-5645.

Li, Z.P. (1992) The genesis of the Rushan gold deposits in east Shandong. Mineral deposits, 11, 165-172 (in Chinese with English abstract).

Luo, X.J., Yang, W.D., Li, R.X., and Gao, L.P. (2001) Effects of pH on the solubility of the Feldspar and the development of secondary porosity. Bulletin of Mineralogy, Petrology and Geochemistry, 20(2), 103-107.

Monecke, T., Kempe, U., and Götze, J. (2002) Genetic significance of the trace element content in metamorphic and hydrothermal quartz: A reconnaissance study. Earth and Planetary Science Letters, 202, 709-724.

Müller, A., Breiter, K., Seltmanna, R., and Pecskay, Z. (2005) Quartz and feldspar zoning in the eastern Erzgebirge volcano-plutonic complex (Germany, Czech Republic): evidence of multiple magma mixing. Lithos, 80, 201-227.

Müller, A., Lennox, P., and Trzebski, R. (2002) Cathodoluminescence and microstructural evidence for crystallisation and deformation processes of granites in the Eastern Lachlan

Fold Belt (SE Australia). Contributions to Mineralogy and Petrology, 143, 510–524.

Müller, A., Seltmann, R., and Behr, H.J. (2000) Application of cathodoluminescence to magmatic quartz in a tin granite: case study from the Schellerhau Granite Complex, Eastern Erzgebirge, Germany. Mineralium Deposita, 35, 169–189.

Naoya, M.,Yoshiaki, Y., and Kuniaki, M. (2005) Successive zoning of Al and H in hydrothermal vein quartz. American Mineralogist, 90(2-3), 310-315.

Olivia, B., Craig, C., and Chad, D. (2020) Quartz crystals in Toba rhyolites show textures symptomatic of rapid crystallization. American Mineralogist, 105, 194-226.

Passchier, C.W. and Trouw, R.A.J. (2005) Microtectonics. Springer, Berlin, Heidelberg, Germany.

Penniston-Dorland, S.C. (2001) Illumination of vein quartz textures in a porphyry copper ore deposit using scanned cathodoluminescence: Grasberg Igneous Complex, Irian Jaya, Indonesia. American Mineralogist, 86, 652–666.

Qiu, K.F., Deng, J., Yu, H.C., Wu, M.Q., Wang, Y., Zhang, L., and Goldfarb, R., 2021. Identifying hydrothermal quartz vein generations in the Taiyangshan porphyry Cu-Mo deposit (West Qinling, China) using cathodoluminescence, trace element geochemistry, and fluid inclusions. Ore Geology Reviews 128: 103882.

Qiu, K.F., Goldfarb, R.J., Deng, J., Yu, H.C, Gou, Z.Y., Ding, Z.J., Wang, Z.K., and Li, D.P., 2020a. Gold deposits of the Jiaodong Peninsula, eastern China. SEG Special Publications 23, 753–773.

Qiu, K.F., Yu, H.C., Deng, J., McIntire, D., Gou, Z.Y., Geng, J.Z., Chang, Z.S., Zhu, R., Li, K.N., and Goldfarb, R.J., 2020b. The giant Zaozigou orogenic Au-Sb deposit in West Qinling, China: Magmatic or metamorphic origin?. Mineralium Deposita, 55(2): 345–362.

Redmond, P.B., Einaudi, M.T., Inan, E.E., Landtwing, M.R., and Heinrich, C.A. (2004) Copper deposition by fluid cooling in intrusion-centered systems: New insights from the Bingham porphyry ore deposit, Utah. Geology, 32, 217–220.

Rusk, B. and Reed, M. (2002) Scanning electron microscope-cathodoluminescence of quartz reveals complex growth histories in veins from the Butte porphyry copper deposit, Montana. Geology, 30, 727-730.

Rusk, B., Koenig, A., and Lowers, H. (2011) Visualizing trace element distribution in quartz using cathodoluminescence, electron microprobe, and laser ablation-inductively coupled plasma-mass spectrometry. American Mineralogist, 96, 703–708.

Rusk, B., Lowers, H., and Reed, M. (2008) Trace elements in hydrothermal quartz; relationships to cathodoluminescent textures and insights into hydrothermal processes. Geology, 36, 547–550.

Sai, S.X., Deng, J., Qiu, K.F., Miggins, D.P., and Zhang, L., 2020. Textures of auriferous quartz-sulfide veins and 40Ar/39Ar geochronology of the Rushan gold deposit: Implications for processes of ore- fluid infiltration in the eastern Jiaodong gold province, China. Ore Geology Reviews, 117: 103254.

Sai, S.X. and Qiu, K.F., 2020. Ore-forming processes of the Rushan gold deposit, Jiaodong: Fluid immiscibility under episodic fluid pressure fluctuations. Acta Petrologica Sinica, 36(5):1547-1566 (in Chinese with English abstract).

Shen, K., Hu, S.X., Sun, J.G., Ling, H.F., Zhao, YY., and Sun, M.Z. (2000) Characteristics of ore-forming fluid of the Dayingezhuang gold deposit in Eastern Shandong, China. Acta Petrologica Sinica 16(04), 542-550 (in Chinese with English abstract).

Thomas, J.B., Watson, E.B., Spear, F.S., Shemella, P.T., Nayak, S.K., and Lanzirotti, A. (2010) TitaniQ under pressure: the effect of pressure and temperature on the solubility of Ti in quartz. Contributions to Mineralogy and Petrology, 160, 743–759.

Wark, D.A. and Watson, B.E. (2006) TitaniQ: A titanium in quartz geothermometer. Contributions to Mineralogy and Petrology, 152, 743–754.

Wang, Y., Qiu, K.F., Hou, Z.L., and Yu, H.C., 2022. Quartz Ti/Ge-P discrimination diagram: A machine learning based approach for deposit classification. Acta Petrologica Sinica, 38(1): 281-290 (in Chinese with English abstract).

Wang, Y., Qiu, K.F., Müller, A., Hou, Z.L., Zhu, Z.H., and Yu, H.C., 2021. Machine learning prediction of quartz forming-environments. Journal of Geophysical Research: Solid Earth, e2021JB021925. https://doi.org/10.1029/2021JB021925.

Watt, G.R., Wright, P., Galloway, S., and McLean, C. (1997) Cathodoluminescence and trace element zoning in quartz phenocrysts and xenocrysts: Geochimica et Cosmochimica Acta, 61, 4337-4348.

Yang, Y., Rainer Abart, Yang, X.S., Shang, Y.M., Theo Ntaflos and Xu, B. (2019) Seismic anisotropy in the Tibetan lithosphere inferred from mantle xenoliths. Earth and Planetary Science Letters, 515, 260-270.

Yu, H.C., Qiu, K.F., Chew, D., Yu, C., Ding, Z.J., Zhou, T., Li, S., and Sun, K.F., 2022. Buried Triassic rocks and vertical distribution of ores in the giant Jiaodong gold province (China) revealed by apatite xenocrysts in hydrothermal quartz veins. Ore Geology Reviews, 140, 104612.

Yu, H.C., Qiu, K.F., Hetherington, C.J., Chew, D., Huang, Y.Q., He, D.Y., Geng, J.Z., and Xian, H.Y., 2021. Apatite as an alternative petrochronometer to trace the evolution of magmatic systems containing metamict zircon. Contributions to Mineralogy and Petrology, 176, 68.

Zeng, Y.J., Li, L., Li, S.R., Santosh, M., and Masroor, A. (2019) The geochemistry of Au–Ag minerals and base-metal sulphides as indicators for gold precipitation: Case study of the Shihu gold deposit, central North China Craton. Geological Journal, 55, 1-15.

Zeng, Y.J. (2019) The terminal effect and signature system of "Jiaodong" type gold deposit: Case study of the Shihu gold deposit, central North China Craton. Ph.D. thesis. China University of Geosciences, Beijing.

Zhai, Y.S., Yao, S.Z., and Cai, K.Q. (2011) Mineral deposits (3rd edition). Geology Press, Beijing, Chinese.

Zhu, X.Y. (1991) Ore-forming physieochemleal environment and enrichment mechanism of the Muping-Rushan gold ore belt. Geology and Exploration, 09, 50-56 (in Chinese with English abstract).

Figure captions

Fig. 1 Geological map of the Muping-Rushan gold belt **(a)** (Deng et al. 2020a) and the Fuping district of the northern Taihang Mountain **(c)**; Cross-section of the orebody No. II in the Rushan gold deposit **(b)** (Li et al. 2015), and No. 101 in the

DOI: https://doi.org/10.2138/am-2022-8471. http://www.minsocam.org/

Shihu gold deposit **(d)** (Li and Santosh 2017; Li et al. 2013)

Fig. 2 Correlations between Al and K in quartz from Shihu **(a)** and Rushan **(b)** Au deposits

Fig. 3 Scanning electron microscope-cathodoluminescence (SEM-CL) images **(a)**, electron probe micro-analysis (EPMA) trace element maps **(b)**, and electron backscatter diffraction (EBSD) maps of quartz from the Shihu and Rushan Au deposit, North China Craton **(c-f)**. IPF: inverse pole figure; KAM: kernel average misorientation; GROD: grain reference orientation deviation

Fig. 4 X-ray diffraction and Fourier transform infrared spectroscopy analyses of different CL zoning in hydrothermal quartz from the Shihu and Rushan Au deposits, projected on the scanning electron microscope-cathodoluminescence images and electron probe micro-analysis trace element mappings; The cell volume and a_0 values of quartz were obtained from the CIF documents using Mercury software

Fig. 5 **(a-d)** TEM and HRTEM images of aluminum-rich bands of quartz from the Shihu and Rushan Au deposits; **(e)(f)** Line scanning of aluminum, potassium, sodium and titanium; **(g)(h)** Structural configuration of trace elements in the quartz atomic lattice (modified after Larsen et al. 2004); **(g)** Coupled substitution of Al^{3+} and H^{+} ions for Si^{4+} i.e. $(Al^{3+}-H^{+})-Si^{4+}$ substitution; **(h)** Coupled substitution of Al^{3+} and K^{+}ions for Si^{4+} i.e. $(Al^{3+}-K^{+})-Si^{4+}$ substitution (the incorporation of Al, H and K is mainly based on the conclusion of this study, Larsen et al. 2004 and Götze, 2009)

Figure.1

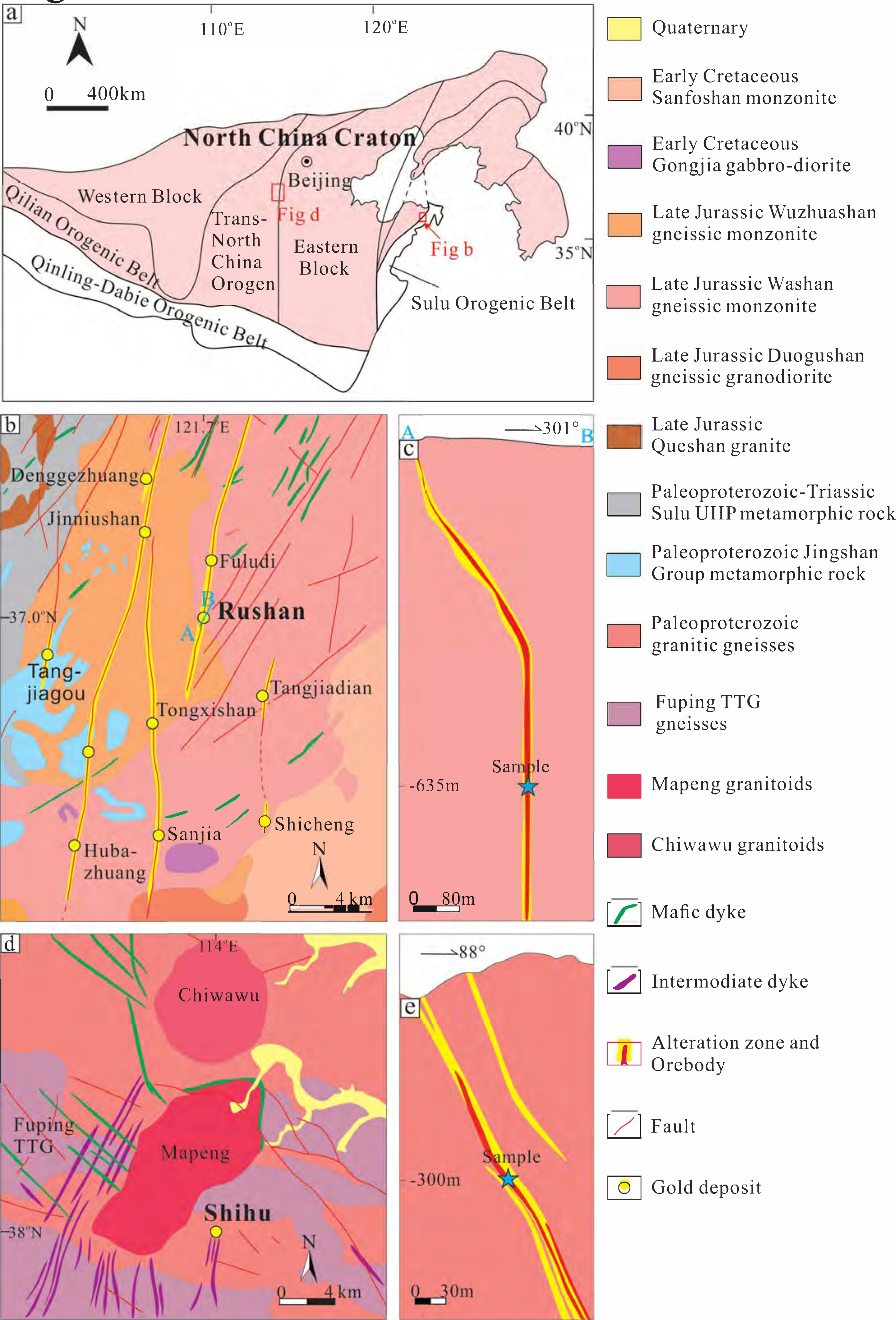

a
N
0 400km
110°E
120°E
40°N
35°N
North China Craton
Beijing
Western Block
Trans-North China Orogen
Fig d
Eastern Block
Fig b
Qilian Orogenic Belt
Qinling-Dabie Orogenic Belt
Sulu Orogenic Belt
b
121.7°E
Denggezhuang
Jinniushan
Fuludi
37.0°N
B
A
Rushan
Tang-jiagou
Tangjiadian
Tongxishan
Sanjia
Shicheng
Huba-zhuang
N
0 4 km
c
A
301°
B
Sample
-635m
0 80m
d
114°E
Chiwawu
Fuping TTG
Mapeng
Shihu
38°N
N
0 4 km
e
88°
Sample
-300m
0 30m
Quaternary
Early Cretaceous Sanfoshan monzonite
Early Cretaceous Gongjia gabbro-diorite
Late Jurassic Wuzhuashan gneissic monzonite
Late Jurassic Washan gneissic monzonite
Late Jurassic Duogushan gneissic granodiorite
Late Jurassic Queshan granite
Paleoproterozoic-Triassic Sulu UHP metamorphic rock
Paleoproterozoic Jingshan Group metamorphic rock
Paleoproterozoic granitic gneisses
Fuping TTG gneisses
Mapeng granitoids
Chiwawu granitoids
Mafic dyke
Intermodiate dyke
Alteration zone and Orebody
Fault
Gold deposit

Figure 2

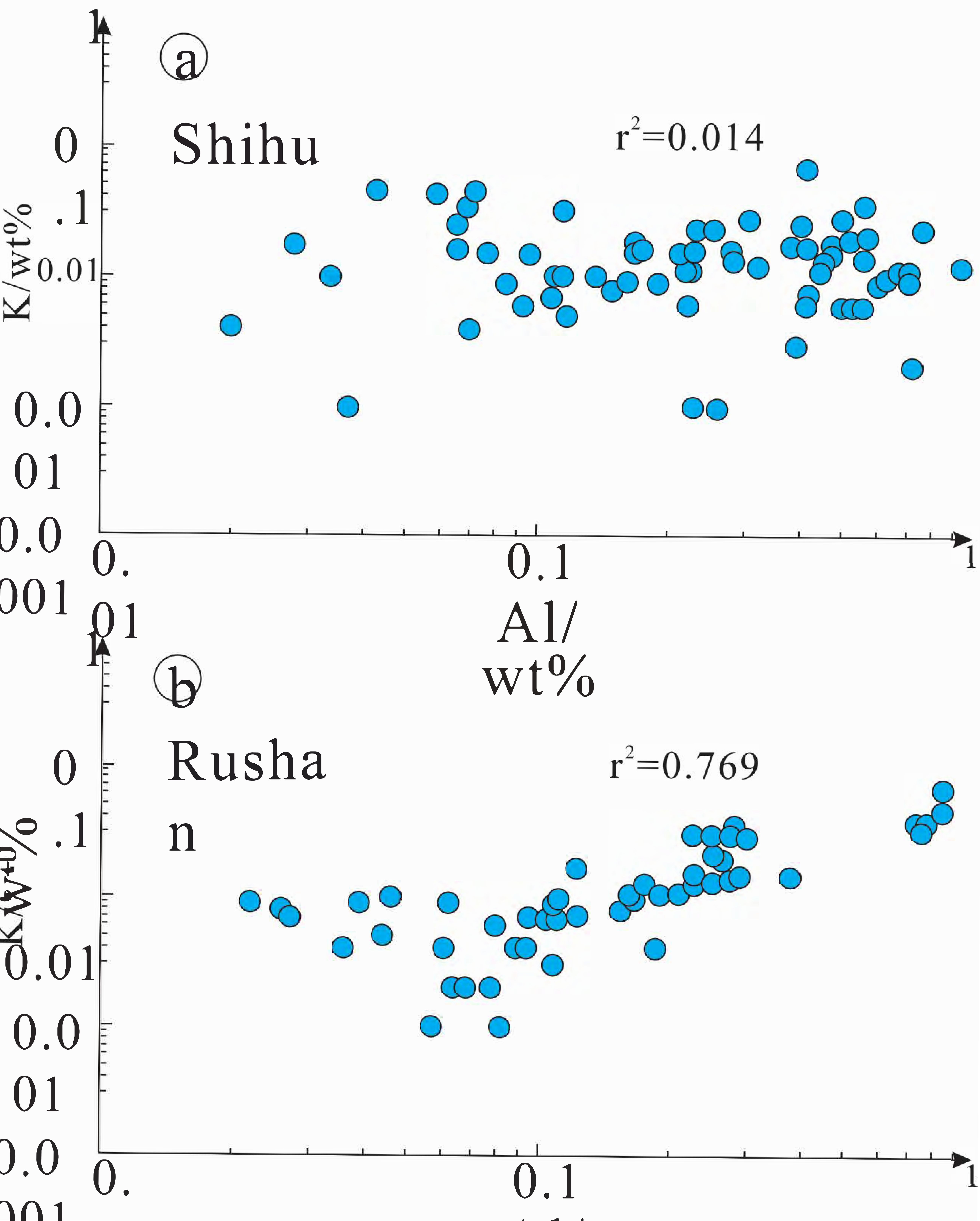

Figure.3

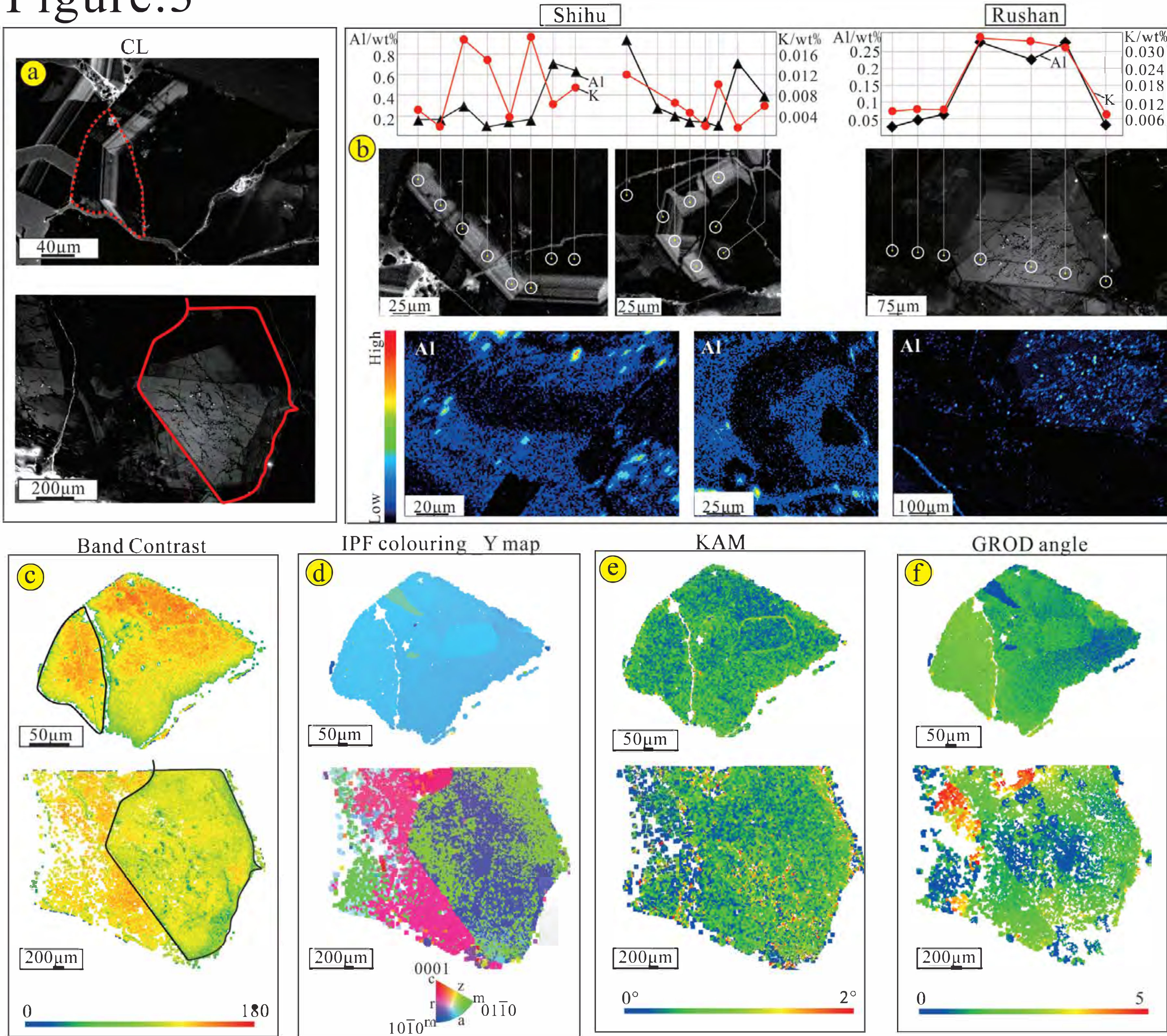

CL
Shihu
Rushan
a
40μm
200μm
Shihu
Rushan
Al/wt%
K/wt%
Al
K
b
25μm
25μm
75μm
High
Low
Al
20μm
25μm
100μm
Band Contrast
IPF colouring _Y map
KAM
GROD angle
c
d
e
f
50μm
200μm
0
180
0001
c
z
m
r
01$\bar{1}$0
10$\bar{1}$0
a
0°
2°
0
5

Figure.4

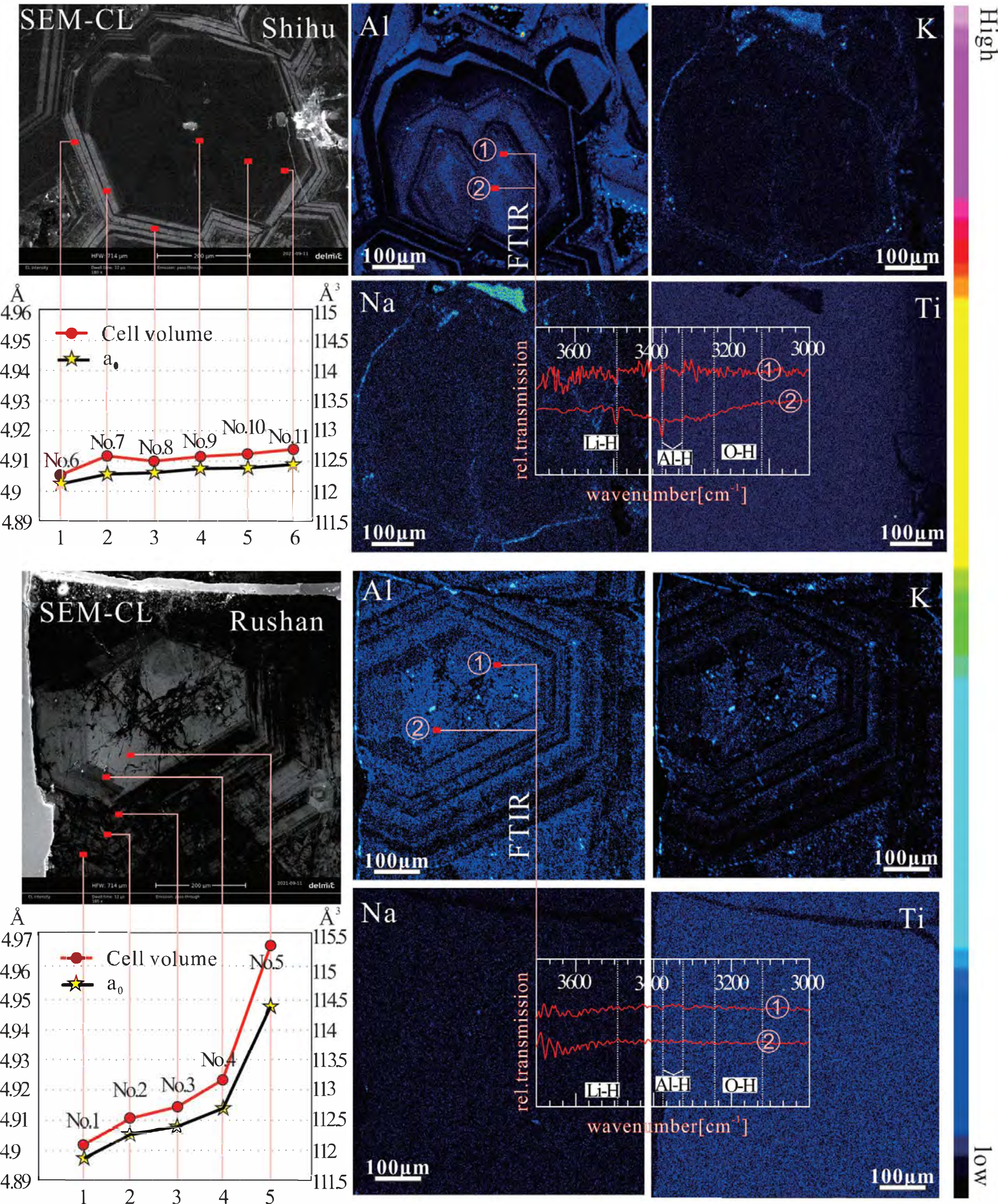

SEM-CL
Shihu
Al
K
High
low
FTIR
100μm
Na
Ti
Cell volume
a_0
No.6
No.7
No.8
No.9
No.10
No.11
rel.transmission
wavenumber[cm^{-1}]
Li-H
Al-H
O-H
SEM-CL
Rushan
No.1
No.2
No.3
No.4
No.5

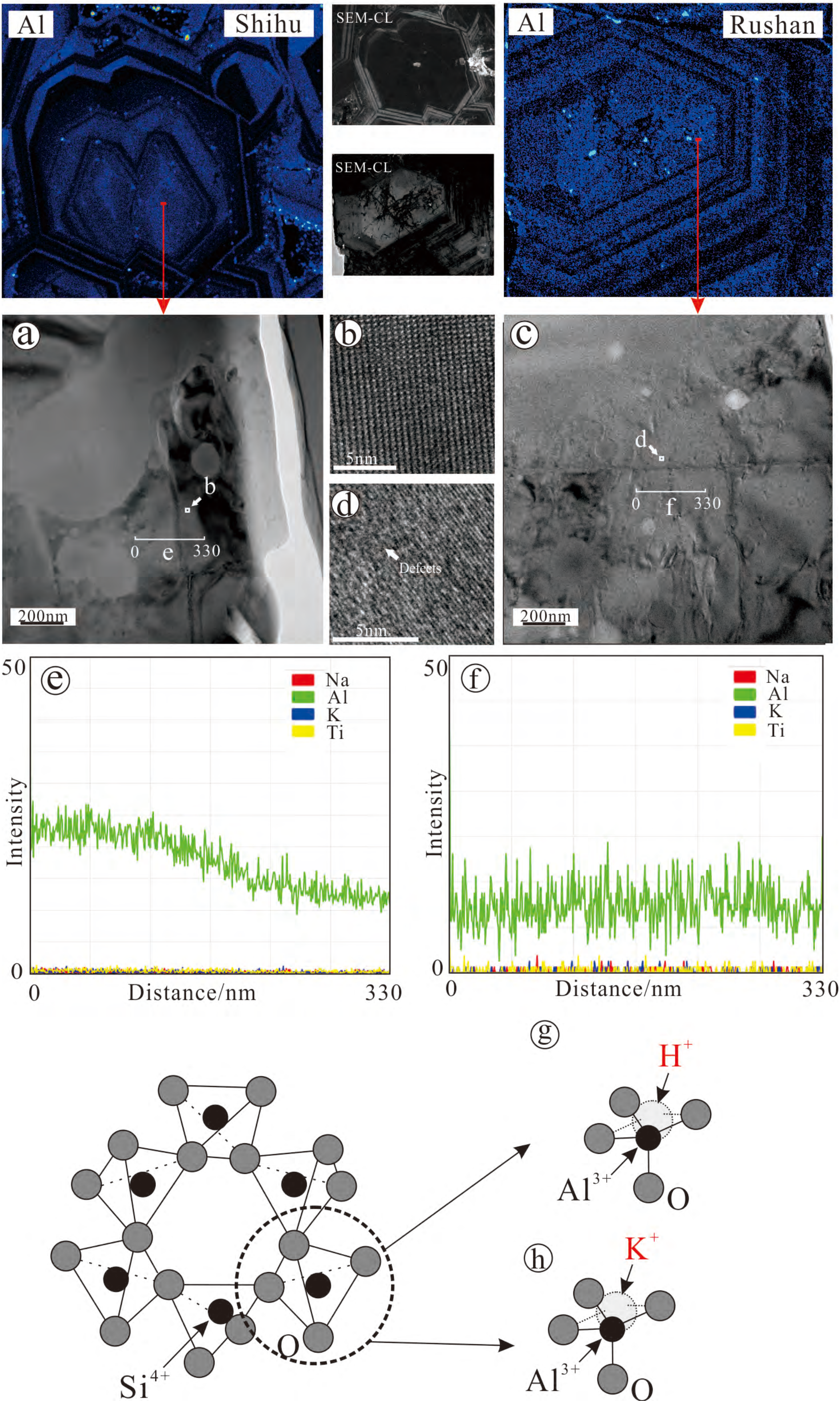
Al
Shihu
SEM-CL
SEM-CL
Al
Rushan
a
b
0
e
330
200nm
b
5nm
d
Defects
5nm
c
d
0
f
330
200nm
e
Na
Al
K
Ti
Intensity
50
0
0
Distance/nm
330
f
Na
Al
K
Ti
Intensity
50
0
0
Distance/nm
330
g
H+
Al3+
O
h
K+
Al3+
O
O
Si4+